Available online at www.sciencedirect.com
SCIENCE DIRECT®
Mechanics of Materials 36 (2004) 893–913
MECHANICS OF MATERIALS
www.elsevier.com/locate/mechmat

Modeling of transformation-induced plasticity and its effect on the behavior of porous shape memory alloys. Part II: porous SMA response

Pavlin B. Entchev, Dimitris C. Lagoudas *

Department of Aerospace Engineering, Texas A&M University, College Station, TX 77843-3141, USA

Received 28 October 2002; received in revised form 4 August 2003

Abstract

The thermomechanical constitutive model for fully dense shape memory alloys (SMAs) developed in Part I [D.C. Lagoudas, P.B. Entchev, to be published. Modeling of transformation-induced plasticity and its effect on the behavior of porous shape memory alloys. Part I: constitutive model for fully dense SMAs, Mechanics of Materials, this issue] of this two-paper series is used in a micromechanical averaging scheme to establish a model for the effective mechanical behavior of porous shape memory alloys. An incremental formulation of the Mori–Tanaka averaging scheme is employed in this work, where the porous material is treated as a two-phase composite with an SMA matrix and the pores as the second phase. The simultaneous development of transformation and plastic strain in the SMA matrix is taken into account. Expressions for the effective elastic and tangent stiffness tensors are presented as well as an expression for the evolution of the effective inelastic strain. The material parameters used by the model are estimated for the case of porous NiTi SMA processed from elemental Ni and Ti powders. Two different porous NiTi alloys are considered in the current work—material with large pore size (~1 mm) and with small pore size (~25 μm). The results of the model simulations for compressive mechanical loading of both types of porous SMAs are compared with the experimental data.

Keywords: Shape memory alloy; Constitutive modeling; Transformation-induced plasticity; Porous SMA; Micromechanical modeling

1. Introduction

Driven by biomedical applications, recent emphasis has been given to *porous SMAs*. The possibility of producing SMAs in porous form opens new fields of application, including reduced weight and increased biocompatibility. Perhaps the most successful application of porous SMAs to this date is their use as bone implants (Shabalovskaya et al., 1994; Ayers et al., 1999; Simske et al., 1997). One of the main reasons for such a success is the biocompatibility of the NiTi alloys used in the above cited works. In addition, the porous structure of the alloys allows ingrowth of the tissue into the implant.

In the last several years since the fabrication techniques for porous SMAs have been

* Corresponding author. Tel.: +1-979-845-1604; fax: +1-979-845-6051.
E-mail addresses: pavlin@aero.tamu.edu (P.B. Entchev), lagoudas@tamu.edu (D.C. Lagoudas).

0167-6636/$ - see front matter © 2003 Elsevier Ltd. All rights reserved.
doi:10.1016/j.mechmat.2003.08.005

established, additional applications have also been considered. The potential applications of porous SMAs utilize their ability to carry significant loads. Beyond the energy absorption capability of dense SMA materials, porous SMAs offer the possibility of higher specific damping capacity under dynamic loading conditions. One of the applications, which utilizes the energy absorption capabilities of porous SMAs, is the development of effective dampers and shock absorbing devices. It has been demonstrated that a significant part of the impact energy is absorbed (Lagoudas et al., 2000). The reason for such high energy absorption is the sequence of forward and reverse phase transformations in the SMA matrix. In addition to the inherent energy dissipation capabilities of the SMA matrix, it is envisioned that the pores will facilitate additional absorption of the impact energy due to wave scattering.

Another advantage of porous SMAs is the possibility to fabricate them with gradient porosity. This porosity gradient offers enormous advantage in applications involving impedance matching at connecting joints and across interfaces between materials with dissimilar mechanical properties. The use of such porous SMA connecting elements will prevent failure due to wave reflections at the interfaces, while at the same time providing the connecting joint with energy absorption capabilities. Also currently of great interest is the use of porous SMAs in various vibration isolation devices. It is envisioned that such devices will find applications in various fields ranging from isolation of machines and equipment to isolation of payloads during launch of space vehicles. To increase the energy absorption capabilities a second phase, which would fill the pores, can also be added. Another advantage of porous SMAs is their lightweight, which would further facilitate their use in space applications.

Finally, it is also envisioned that the porous SMAs may be utilized as multifunctional materials. One such application is to use the pores and the connecting channels for fluid transport, which will provide active cooling/heating of the porous SMA. Another possible application is to design a porous SMA filter and control its temperature to vary the diameter of the channels for fluid flow. It should be noted that these latest developments are still being actively researched and have not yet been used in commercial applications.

In addition to the models developed for fully dense SMAs and reviewed in Part I, models for porous SMAs have started to appear during recent years. Recent achievements in this area are briefly summarized below. Since a porous SMA can be viewed as a composite with an SMA matrix and the pores as the second phase, the models presented for active SMA-based composites are also reviewed.

A great number of research papers have appeared in the literature devoted to modeling of porous materials. While some of them deal with the elastic response of the materials, the inelastic and more specifically, plastic behavior has also been a topic of research investigations. Different aspects of modeling of porous and cellular solids are presented by Green (1972), Gurson (1977), Jeong and Pan (1995) and Gibson and Ashby (1997), among others. The idea behind the works of Green (1972) and Gurson (1977) is to derive a macroscopic constitutive model with an effective yield function for the onset of plasticity. In addition, the work of Gurson (1977) deals with the nucleation and evolution of porosity during loading. A comprehensive study on porous and cellular materials is presented in the book by Gibson and Ashby (1997). However, most of the modeling in that work is presented in the context of a single cell modeling for high-porosity materials. The cells are modeled using the beam theory to account for the ligaments between the pores. In addition, the walls of the pores in the case of closed cell porosity are modeled as membranes. Both the elastic properties as well as the initiation of plasticity are modeled.

Since the emerging of the SMA-based active composites their modeling has been the subject of a number of research papers. One approach to modeling of these composites is to extend the theories for linear composites, which is well developed (e.g., see the review papers by Willis (1981, 1983) and the monograph by Christensen (1991)).

Some of the modeling work on SMA composites has been performed using the approximation of an existence of a periodic unit cell (Achenbach and Zhu, 1990; Nemat-Nasser and Hori, 1993;

Lagoudas et al., 1996). One of the recent works on porous SMAs also used the unit cell approximation to evaluate the properties of porous SMAs (Qidwai et al., 2001). Even though the existence of periodic arrangement of pores in a real porous SMA material is an approximation, this assumption provides insight into global material behavior in the form of useful limiting values for the overall properties. Additionally, an approximate local variation of different field variables like stress and strain indicating areas of concentration due to porosity can be obtained. These results may provide design limitations in order to minimize or even avoid microbuckling, plastic yielding and consequently loss of phase transformation capacity over number of loading cycles. The assumption of periodicity and symmetry boundary conditions reduce the analysis of the porous SMA material to the analysis of a unit cell. In addition, appropriate loading conditions need to be applied, which do not violate the symmetry of the problem (Qidwai et al., 2001). In a recent work DeGiorgi and Qidwai (2001) have investigated the behavior of porous SMA using a mesoscale representation of the porous structure and have also studied the effect of filling the pores with a second polymeric phase.

Micromechanical averaging techniques have also been used to determine the averaged macroscopic composite response. Among the micromechanics averaging methods, the two most widely used are the self-consistent method and the Mori–Tanaka method. Both approaches are based on the presumption that the effective response of the composite can be obtained by considering a single inhomogeneity embedded in an infinite matrix. According to the self-consistent method (Hershey, 1954; Kröner, 1958; Budiansky, 1965; Hill, 1965) the interactions between the inhomogeneities are taken into account by associating the properties of the matrix with the effective properties of the composite, i.e., embedding the inhomogeneity in an effective medium. Some self-consistent results for spherical pores in an incompressible material are presented by Budiansky (1965). Contrary to this approach, the Mori–Tanaka method initially suggested by Mori and Tanaka (1973) and further developed by Weng (1984) and Benveniste (1987) takes into account the interactions between the inhomogeneities by appropriately modifying the average stress in the matrix from the applied stress, while the properties of the matrix are associated with the real matrix phase. These averaging techniques can also be used to determine the averaged macroscopic response of the porous material with random distribution of pores. In this case the material is treated as a composite with two phases: dense matrix and pores.

Recently, both averaging approaches have been applied to obtain effective properties of composites with inelastic phases. For example, a variant of the self-consistent method using incremental formulation (Hutchinson, 1970) has been used to model composites undergoing elastoplastic deformations. Lagoudas et al. (1991) have used an incremental formulation of the Mori–Tanaka method to obtain the effective properties of a composite with an elastoplastic matrix and elastic fibers. Boyd and Lagoudas (1994) have applied the Mori–Tanaka micromechanical method to model the effective behavior of a composite with elastomeric matrix and SMA fibers and have obtained the effective transformation temperatures for the composite. In a different work, Lagoudas et al. (1994) have applied the incremental Mori–Tanaka method to model the behavior of a composite with elastic matrix and SMA fibers. Another group of researchers (Cherkaoui et al., 2000) has applied the self-consistent technique to obtain the effective properties of a composite with elastoplastic matrix and SMA fibers. A two-level micromechanical method has been presented by Lu and Weng (2000), where the SMA constitutive behavior has been derived at the microscopic level and the overall composite behavior has been modeled at the mesoscale level using the Mori–Tanaka method.

In a previous work (Entchev and Lagoudas, 2002) the authors have presented a model for porous SMAs derived using micromechanical averaging techniques. The model was derived by treating the porous SMA as a two-phase composite, with a dense SMA matrix and a second phase to represent the pores. A thermomechanical constitutive model was utilized to model the response of the SMA matrix. However, the model used by Entchev and Lagoudas (2002) did not

account for the development of permanent plastic strains in the dense SMA matrix.

The experimental observations for the mechanical behavior of porous SMAs in the pseudoelastic regime have shown that a significant part of the developed strain is not recovered upon unloading. Even upon heating the specimen in a furnace with no load applied this unrecoverable strain remains unchanged. Thus, the development of this strain has been attributed to plasticity (Lagoudas and Vandygriff, 2003). As shown in Part I of the current work (Lagoudas and Entchev, to be published), similar effects have been observed during mechanical testing of fully dense SMAs.

In the current Part II of this two-part series, the behavior of the porous SMA will be modeled. The micromechanical model presented by Entchev and Lagoudas (2002) will be used. The dense SMA matrix will be modeled using the constitutive model for SMA developed in Part I of this work, while the inhomogeneities will be treated as elastic phases with stiffness equal to zero. The properties of two different porous NiTi SMAs will be established and the results from the numerical simulations will be compared to the experimental results.

The remainder of the paper is organized as follows: the micromechanical averaging model for porous SMAs will be briefly summarized in Section 2. The estimation of the material parameters for the porous NiTi SMA and results for numerical simulation of various boundary value problems for porous SMA bars will be presented in Section 3. A summary of the results and conclusions are presented in Section 5.

The direct notation is adopted in this work. Capital bold Latin letters represent fourth-order tensors (effective stiffness $\mathbf{L}$, compliance $\mathbf{M}$, etc.) while bold Greek letters are used to denote second-order tensors—lower case for the local quantities (stress $\boldsymbol{\sigma}$, strain $\boldsymbol{\varepsilon}$) and capital for the macroscopic quantities (effective stress $\boldsymbol{\Sigma}$, strain $\mathbf{E}$). Regular font is used to denote scalar quantities as well as the components of the tensors. Multiplication of two fourth-order tensors $\mathbf{A}$ and $\mathbf{B}$ is denoted by $\mathbf{AB} = (AB)_{ijk\ell} \equiv A_{ijpq}B_{pqk\ell}$, while the operation ":" defines contraction of two indices when a fourth-order tensor acts on a second-order one, $\mathbf{A} : \mathbf{E} \equiv A_{ijk\ell}E_{k\ell}$.

To distinguish between the references from the current Part II and previous Part I (Lagoudas and Entchev, to be published) of this two-part paper, the references from Part I in the current work will have the prefix "I". For example, Section I-1 will refer to Section 1 of Part I.

2. Modeling of porous shape memory alloys using micromechanical averaging techniques

The model for porous SMAs presented by Entchev and Lagoudas (2002) is utilized in the current work. The behavior of the SMA matrix is modeled using the constitutive model presented in the previous section. An overview of the main results of the model presented by Entchev and Lagoudas (2002) is given below.

2.1. Modeling of the effective behavior of porous SMAs

The model treats the porous SMA as a two-phase composite material with an SMA matrix and second phase representing the pores. The Cauchy stress in the matrix is denoted by $\boldsymbol{\sigma}^m$, the linearized strain is $\boldsymbol{\varepsilon}^m$ and the inelastic strain is $\boldsymbol{\varepsilon}^{\text{in},m}$. Note that the inelastic strain in the matrix may contain both transformation and plastic components. The matrix is characterized by its elastic stiffness $\mathbf{L}^m$ (compliance $\mathbf{M}^m = (\mathbf{L}^m)^{-1}$) and tangent stiffness $\mathbf{T}^m$. The volume fraction of the matrix phase is c^m and the volume fraction of the pores is $c^i = 1 - c^m$. The porous SMA is characterized by its effective elastic stiffness $\mathbf{L}$, tangent stiffness $\mathbf{T}$ and effective stress, strain and inelastic strain $\boldsymbol{\Sigma}$, $\mathbf{E}$ and $\mathbf{E}^{\text{in}}$. A detailed derivation of the micromechanical model is presented by Entchev and Lagoudas (2002) and only the expressions for the effective elastic stiffness $\mathbf{L}$, tangent stiffness $\mathbf{T}$ and the increment of the effective inelastic strain $\dot{\mathbf{E}}^{\text{in}}$ are presented here.

To connect the macroscopic strain rate to the microscopic one, two types of strain concentration factors are defined. The *instantaneous* strain concentration factor $\mathscr{A}(\mathbf{x})$ is defined as (assuming that the local strain is driven by the macroscopic strain):

$$\dot{\boldsymbol{\varepsilon}} = \mathscr{A}(\mathbf{x}) : \dot{\mathbf{E}}. \tag{1}$$

The tensor $\mathscr{A}(\mathbf{x})$ is generic and takes different values in different phases such that

$$\mathscr{A}(\mathbf{x}) = \begin{cases} \mathbf{A}^m(\mathbf{x}), & \mathbf{x} \in V^m; \\ \mathbf{A}^i(\mathbf{x}), & \mathbf{x} \in V^i. \end{cases} \tag{2}$$

The *elastic* strain concentration factor $\mathscr{A}^{\mathrm{el}}(\mathbf{x})$ is similar to the instantaneous strain concentration factor but is defined for the case of elastic loading (unloading).

Thus, the overall elastic stiffness $\mathbf{L}$ is given by

$$\mathbf{L} = c^m \mathbf{L}^m \mathbf{A}^{\mathrm{el},m}, \tag{3}$$

where $\mathbf{A}^{\mathrm{el},m}$ is the average *elastic* strain concentration factor for the matrix:

$$\mathbf{A}^{\mathrm{el},m} = \frac{1}{V^m} \int_{V^m} \mathscr{A}^{\mathrm{el}}(\mathbf{x}) \, \mathrm{d}V. \tag{4}$$

The expression for the elastic stiffness (3) is well-known and presented in the literature (see, for example the works of Hill, 1963; Weng, 1984; Benveniste, 1987).

Next, an expression for the overall tangent stiffness $\mathbf{T}$ is given:

$$\mathbf{T} = c^m \mathbf{T}^m \mathbf{A}^m, \tag{5}$$

where $\mathbf{A}^m$ is the average *instantaneous* strain concentration factor for the matrix. In the case of elastic behavior the above expression for the macroscopic tangent stiffness will take the same form as the expression for the macroscopic elastic stiffness.

The next step in establishing the macroscopic constitutive behavior of the composite is the derivation of an evolution equation for the macroscopic inelastic strain $\mathbf{E}^{\mathrm{in}}$. The expression for $\dot{\mathbf{E}}^{\mathrm{in}}$ is given by:

$$\begin{aligned} \dot{\mathbf{E}}^{\mathrm{in}} = {} & \dot{\mathbf{E}} - c^m \mathbf{M} \mathbf{L}^m : (\mathbf{A}^m : \dot{\mathbf{E}} - \langle \dot{\boldsymbol{\varepsilon}}^{*m} \rangle_m) \\ & - \dot{\mathbf{M}} \mathbf{L} : (\mathbf{E} - \mathbf{E}^{\mathrm{in}}), \end{aligned} \tag{6}$$

where the quantity $\dot{\boldsymbol{\varepsilon}}^{*m}$ is given by

$$\dot{\boldsymbol{\varepsilon}}^{*m} = \dot{\boldsymbol{\varepsilon}}^{\mathrm{t},m} + \dot{\boldsymbol{\varepsilon}}^{p,m} + \dot{\mathbf{M}}^m : \boldsymbol{\sigma}^m, \tag{7}$$

and the subscript m indicates that the volume average is taken over the matrix phase V^m. The above Eq. (6) is a first order ODE for $\mathbf{E}^{\mathrm{in}}$. Since the coefficients of this equation (overall elastic compliance, elastic stiffness of the matrix as well as the concentration factor) change during the phase transformation, they ultimately depend on $\mathbf{E}^{\mathrm{in}}$. Thus this equation is non-linear and cannot be integrated directly for given history of the overall strain $\mathbf{E}$.

Thus, expressions for the overall elastic stiffness $\mathbf{L}$, overall tangent stiffness $\mathbf{T}$ and the evolution of the overall inelastic strain $\mathbf{E}^{\mathrm{in}}$ which fully characterize the behavior of a porous SMA are derived.

2.2. Evaluation of the strain concentration factors

The Mori–Tanaka method is used in this work to calculate the concentration factors. One of the reasons for choosing the Mori–Tanaka method is the fact that in porous SMAs the matrix is readily identified. Another reason is its relative simplicity, compared to the self-consistent method, which is implicit. For the case of ellipsoidal inhomogeneities the Mori–Tanaka estimate of $\mathbf{A}^i$ (see Lagoudas et al., 1991) is given by

$$\mathbf{A}^i = [\mathbf{I} + c^m \mathbf{S}^{\mathrm{E}}]^{-1}, \tag{8}$$

where $\mathbf{S}^{\mathrm{E}}$ is the Eshelby tensor, which is defined for the shape of inhomogeneities and the matrix tangent stiffness. Using the well-known identity $c^m \mathbf{A}^m + c^i \mathbf{A}^i = \mathbf{I}$ the average strain concentration factor for the matrix is given by

$$\mathbf{A}^m = \frac{1}{c^m} (\mathbf{I} - c^i \mathbf{A}^i). \tag{9}$$

The estimates of the average elastic strain concentration factors $\mathbf{A}^{\mathrm{el},m}$ and $\mathbf{A}^{\mathrm{el},i}$ used in the evaluation of the macroscopic elastic stiffness $\mathbf{L}$ are obtained as

$$\mathbf{A}^{\mathrm{el},i} = [\mathbf{I} + c^m \mathbf{S}^{\mathrm{E,el}}]^{-1}, \tag{10}$$

$$\mathbf{A}^{\mathrm{el},m} = \frac{1}{c^m} (\mathbf{I} - c^i \mathbf{A}^{\mathrm{el},i}). \tag{11}$$

The quantity $\mathbf{S}^{\mathrm{E,el}}$ in the equation above is the Eshelby tensor evaluated using the elastic stiffness of the matrix.

To evaluate the Eshelby tensor, the shape of the pores must be specified. A study on the effect of different ellipsoidal pore shapes on the effective properties has been presented by Entchev and

Lagoudas (2002). It has been concluded that a spherical pore shape gives adequate representation of random distribution of pores and at the same time its use greatly reduces computational costs. Thus, a spherical pore shape will also be used in this work.

2.3. Inelastic strain evolution during phase transformation

To demonstrate the capabilities of the model numerical calculations for porous SMA undergoing phase transformation have been performed. As a starting point, first the response during stable transformation cycle is modeled. To accomplish this task, the material parameters for the SMA matrix are selected to correspond to NiTi characterized in the work of Bo et al. (1999). These material parameters are presented in Table I-1. Note that these parameters are for stable transformation cycle.

The developed model is implemented as a user material subroutine (UMAT) in ABAQUS (HKS, 1997). The material subroutine developed in Part I is expanded to take into account the micro-mechanical averaging and the evaluation of the macroscopic transformation strain.

As a representative example, numerical evaluations for the isothermal pseudoelastic response of porous NiTi SMA were performed. The temperature was set to be 343 K. The numerical calculations were performed for an SMA prismatic bar under uniaxial loading. The numerical results were produced using a mesh of two 3-D eight node solid elements, while identical results were obtained for a mesh of eight 3-D elements, since both stress and strain are uniform. The axial effective stress–strain response of the bar for various levels of porosity $c^{\mathrm{p}} = 1 - c^m$ is shown in Fig. 1.

Next, the solution of Eq. (6) during phase transformation is investigated. For convenience equation (6) is shown below, where different components contributing to the overall inelastic strain are identified:

$$\dot{\mathbf{E}}^{\mathrm{in}} = \underbrace{\left(\mathbf{I} - \left(\mathbf{A}^{\mathrm{el},m}\right)^{-1}\mathbf{A}^{m}\right) : \dot{\mathbf{E}}}_{\text{term 1}} + \underbrace{\left(\mathbf{A}^{\mathrm{el},m}\right)^{-1} : \left\langle \dot{\boldsymbol{\varepsilon}}^{*m} \right\rangle_{m}}_{\text{term 2}} - \underbrace{\dot{\mathbf{M}} : \boldsymbol{\Sigma}}_{\text{term 3}} \tag{12}$$

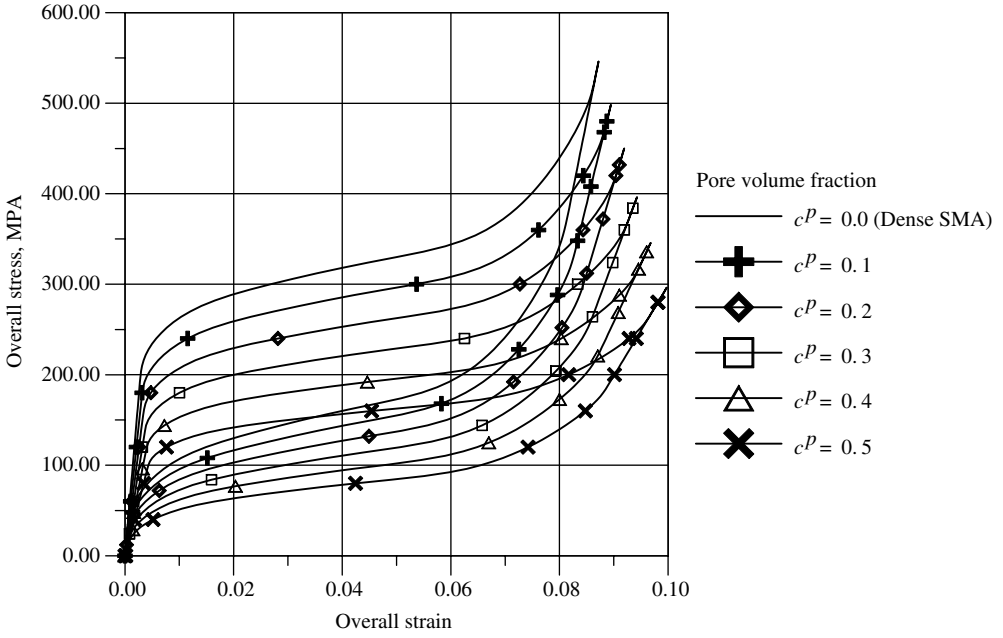

Fig. 1. Effective stress–strain response of a porous NiTi SMA bar.

It can be seen from Eq. (12) that there are three terms contributing to the macroscopic inelastic strain. The first term is due to the difference between the elastic and instantaneous strain concentration factors. In the case that $\mathbf{A}^{\mathrm{el},m}$ and $\mathbf{A}^{m}$ are the same this term will vanish. The second term represents the effect of the inelastic strain rate $\langle \dot{\boldsymbol{\varepsilon}}^{*m} \rangle_m$ in the matrix, which has three contributions, one from the transformation strain, the second from the plastic strain and the third from the stiffness change in the matrix (see Eq. (7)). Note that the inelastic strain rate is multiplied by the inverse of the elastic strain concentration factor $(\mathbf{A}^{\mathrm{el},m})^{-1}$. The third term is due to the change in the effective elastic compliance during the phase transformation.

The contribution of each of the three terms to the macroscopic inelastic strain $\mathbf{E}^{\mathrm{in}}$ is examined for three different cases. The calculations for all of the three cases are performed on a uniaxial SMA bar with 50% porosity for the loading path shown in Fig. 2. The difference between the three test cases is in the properties of the SMA matrix.

In the first case it is assumed that the SMA matrix undergoes phase transformation and no plastic strains are accumulated. This case describes the situation where the SMA matrix undergoes a stable transformation cycle. Therefore, the overall inelastic strain $\mathbf{E}^{\mathrm{in}}$ becomes simply the overall transformation strain $\mathbf{E}^{\mathrm{t}}$. The material properties for this test case are the same used to obtain the results shown in Fig. 1 and are summarized in Table I-1. The temperature for this case was set to be 343 K. The normal components in the direction of the loading for each of the three terms contributing to the effective transformation strain are plotted in Fig. 3. It can be seen that the contribution of the second term due to the local transformation strain is dominant for the current choice of the material parameters. The contribution of the first term is negative and lowers the value of the effective macroscopic transformation strain. It can thus be seen from the figure that the effect of the difference between the elastic and instantaneous strain concentration factors is not negligible. The third term, which reflects the effect of the effective elastic compliance change has the smallest magnitude of the three terms. Even though the third term is positive because the elastic compliance of the SMA matrix in the martensitic phase is greater than the compliance in the austenitic phase, its contribution to the total transformation strain is negative, due to the negative sign in front of the term in Eq. (12). It is noted that at the end of the reverse transformation the two contributions of the second and the third terms cancel each other, while the contribution of the first term goes to zero. It can be shown analytically that for the case of porous SMAs the part of the second term, corresponding to the change in the stiffness in the SMA matrix, is exactly equal to the third term. However, this result is only valid for a particular choice of the phases, i.e., martensite and austenite have the same Poisson's ratio, and it will not hold in general.

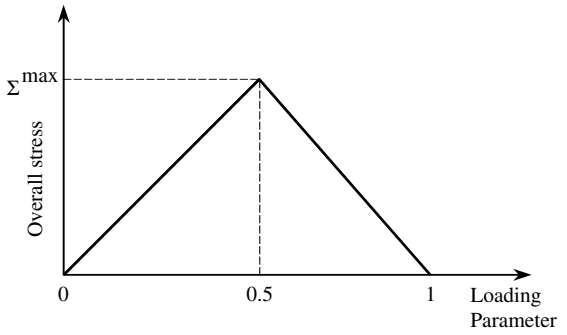

Fig. 2. Loading history for uniaxial porous SMA bar.

In the second test case it is assumed that the elastic properties of the martensite and the austenite are the same, i.e., $\mathbf{M}^{\mathrm{M}} = \mathbf{M}^{\mathrm{A}}$. Then, the rate of inelastic strain in the SMA matrix $\langle \dot{\boldsymbol{\varepsilon}}^{*m} \rangle_m$ becomes simply the rate of the transformation strain $\langle \dot{\boldsymbol{\varepsilon}}^{\mathrm{t},m} \rangle_m$ in the second term, and the third term vanishes. To illustrate this special case, the results of numerical calculations are show in Fig. 4 for the same porous SMA uniaxial bar with porosity of 50% as in the previous case. The material parameters for this case are the ones shown in Table I-2 or NiTi SMA tested by Strnadel et al. (1995). The temperature of the test was set to be 300 K. The values after the stabilization of the transformation cycle (final values) of the material parameters are used. The resulting normal strain components are shown in Fig. 4. The same general trend as in the

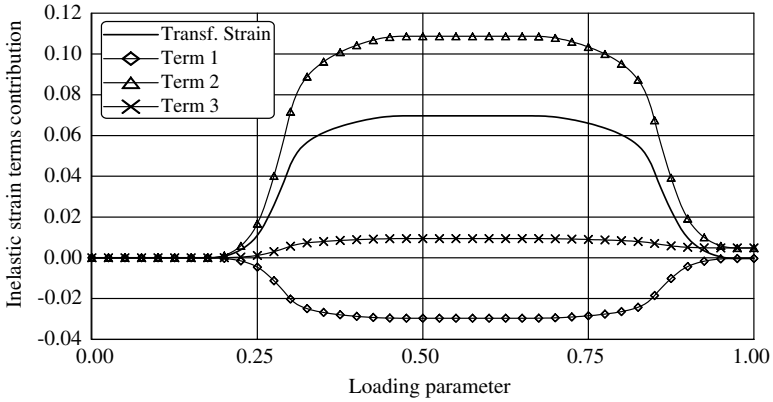

Fig. 3. Components of the macroscopic transformation strain as a function of the loading.

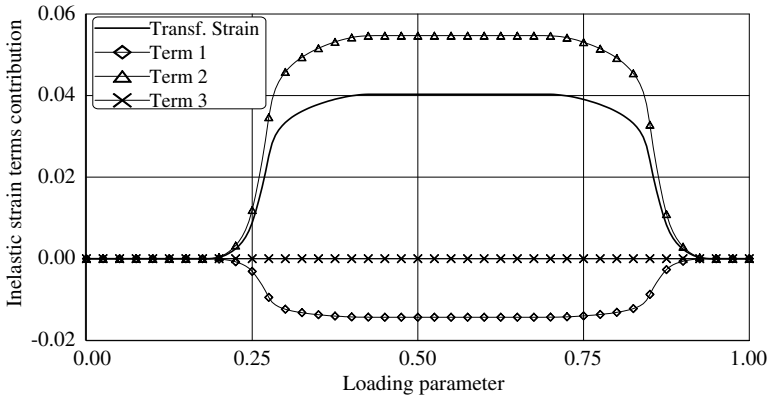

Fig. 4. Components of the macroscopic transformation strain for the case of equal stiffness of the austenite and martensite.

previous case is observed (see Fig. 3). However, in this case the third term in Eq. (12) is zero.

The third test case is an extension of the second case and considers the situation where both transformation and plastic strain are present. Thus, the inelastic strain rate term in the SMA matrix contains both the rate of transformation strain and the rate of plastic strain. To perform the numerical calculations for this test case the same material properties as in the previous case are used (see Table I-2). However, to be able to model the development of plastic strains both the initial and final sets of parameters are used. Numerical simulations of one full transformation cycle are performed at a temperature of 300 K.

The results showing the contribution of the different term on the overall inelastic strain $\mathbf{E}^{\text{in}}$ are shown in Fig. 5. Two effects manifesting the influence of the plastic strain on the development of the overall inelastic strain are observed. First, since the rate of the plastic strain in the matrix $\dot{\boldsymbol{\varepsilon}}^{p,m}$ enters the second term in Eq. (12) it is seen that its contribution at the end of the loading–unloading cycle does not vanish. The second effect is due to the different tangent stiffness during loading and unloading. The difference in the tangent stiffness is caused by the development of the plastic strain and it results in different evaluations of the instantaneous matrix strain concentration factor $\mathbf{A}^m$ during loading and unloading. Therefore, it is seen

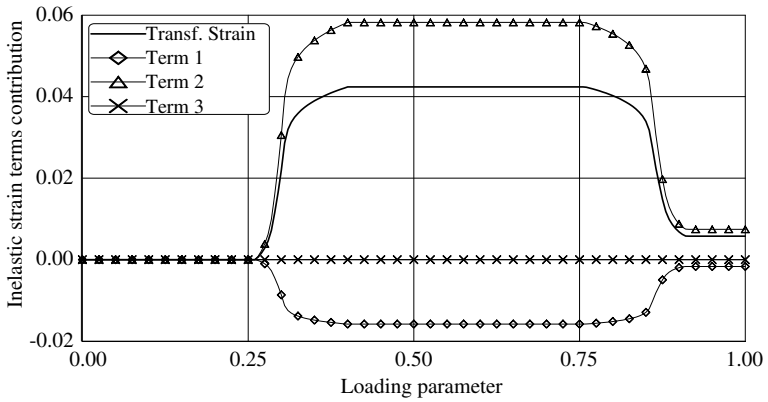

Fig. 5. Components of the macroscopic inelastic strain as a function of the loading (both plastic and transformation strains are present).

that the total contribution of the first term (cf. Eq. (12)) at the end of the transformation cycle does not vanish. These two effects result in the development of non-zero total inelastic strain $\mathbf{E}^{in}$ at the end of the loading–unloading cycle. To better illustrate the situation, the stress–strain curve for this test case is shown in Fig. 6. The residual macroscopic strain at the end of the cycle (at zero applied stress) seen in the figure is caused by the two effects discussed here.

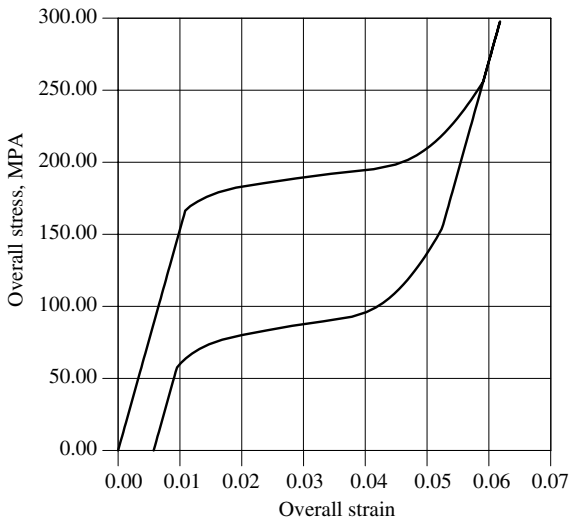

Fig. 6. Effective stress–strain response of a porous NiTi SMA bar (both plastic and transformation strains are present).

3. Estimation of the material parameters and simulation of the response of porous NiTi bars

Porous NiTi specimens were fabricated from elemental Ni and Ti powders using HIPping techniques in the Active Materials Laboratory at Texas A&M University (Vandygriff et al., 2000). Using two slightly different processing cycles two different porous NiTi alloys were produced. The first alloy was fabricated at a temperature of ≈940 °C and is characterized by its small pore size (on the order of 25 μm). The fabrication temperature for the second alloy was ≈1000 °C and the sizes of its pores are significantly larger (pores as large as 1 mm are observed). A detailed analysis of the composition of the two alloys was performed by Lagoudas and Vandygriff (2003) using energy-dispersive X-ray spectrometry (EDS) and further using wave-dispersive X-ray spectrometry (WDS). The analysis has revealed evidence of multiple intermetallic phases present in both large and small pore alloys. The greater part of the material for large pore alloys was identified as equiatomic NiTi. However, the material contains numerous needle-like structures having a width of approximately one-half micron. These needle-like structures were too small to be analyzed without interference from the surrounding medium. By analyzing some of the larger intersections of needle-like phases however, it is presumed by a slight increase in the percentage of Ni that the needle

phases are Ni rich phases. For the small pore alloy five different phases, i.e., NiTi, Ni_2Ti, $NiTi_3$ and elemental Ni and Ti were identified. The apparent reason for the presence of relatively large intermetallic phase regions in the small pore alloy is the lower fabrication temperature, which leads to incomplete diffusion of the elemental powders.

The porosity of the specimens was measured by taking micrographs and estimating the ratio of the area occupied by the pores to the total area at different cross-sections. The estimate of the porosity was also verified by comparing the density of the porous NiTi material with the theoretical density of fully dense NiTi. The porosity of the small pore alloy is estimated to be equal to 50% while the porosity of the large pore alloy is equal to 42%. Micrographs of typical specimens for both small and large pore alloys are shown in Figs. 7 and 8. The dark areas on the micrographs, shown in Figs. 7 and 8 represent the pores, while the lighter areas are occupied by NiTi.

The porous NiTi specimens were further analyzed using differential calorimetry techniques. The DSC test curves for both small and large pore alloys are shown in Figs. 9 and 10, respectively. The upper curves seen in Figs. 9 and 10 represent the normalized heat flow into the specimen during heating and the lower curves represent the heat flow out of the specimen upon cooling. The tests indicate solid–solid phase transformation at approximately 44 and 42 °C for the small and large pore alloys during heating (martensite-to-austenite) and

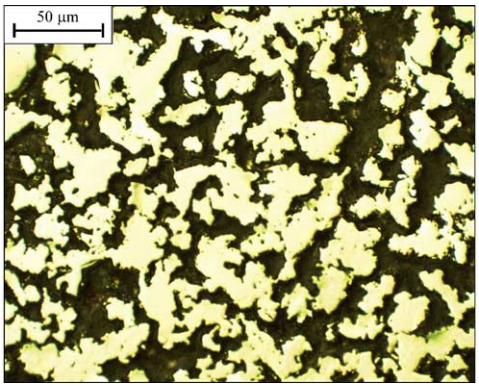

Fig. 7. Microphotograph of a small pore porous NiTi specimen.

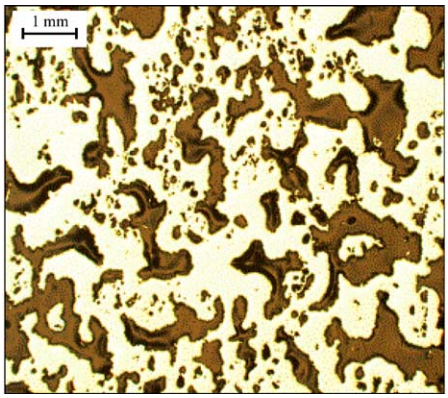

Fig. 8. Microphotograph of a large pore porous NiTi specimen.

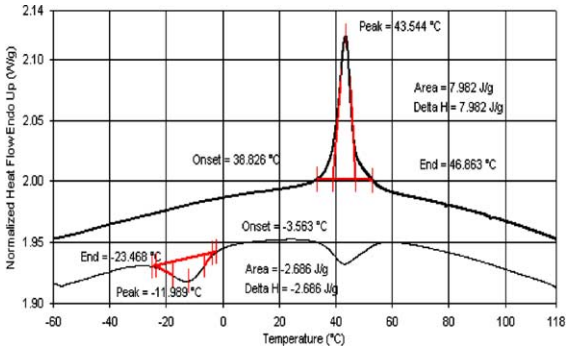

Fig. 9. DSC results for small pore porous NiTi alloy.

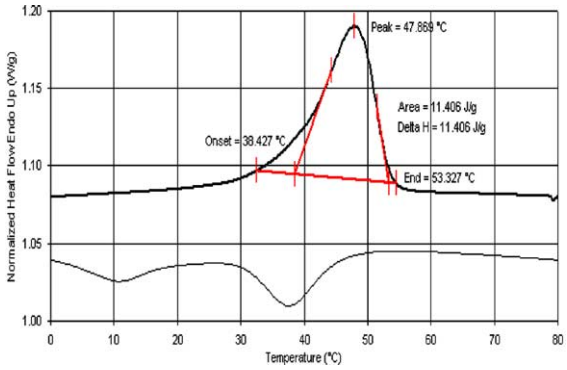

Fig. 10. DSC results for large pore porous NiTi alloy.

−12 and 20 °C during cooling (austenite-to-martensite) for the small and large pore specimens, respectively. Therefore, depending on whether the

specimen was previously heated or cooled, either martensite or austenite crystalline structure can be present at room temperature (22 °C). The cooling curves for both alloys show evidence of a dual peak that is indicative of an *R*-phase.

The fabricated porous NiTi specimens have a cylindrical shape with a nominal diameter of 13 mm and a length of 35 mm. The specimens were mechanically tested under compressive load. Load from a hydraulic MTS load frame was applied through two compression plates. An extensometer was used to take the strain measurements during testing. The specimens were tested using a cyclic loading–unloading pattern by loading quasi-statically up to a stress and strain level and then unloading to zero stress. For each subsequent cycle, the stress and/or strain were increased with respect to the previous level. The resulting stress–strain response for a typical small pore specimen, tested at a temperature of 60 °C is shown in Fig. 11 and shows evidence of pseudoelastic behavior upon unloading. However, full strain recovery is not observed, which is due to plastic strain development in the SMA matrix. The typical stress–strain response for a large pore specimen also tested at 60 °C is shown in Fig. 12. The results for the second specimen are qualitatively similar to the result for the small pore specimen. However, certain distinctions are observed from Figs. 11 and 12. The initial tangent stiffness of the austenite and martensite are different in the two specimens. The

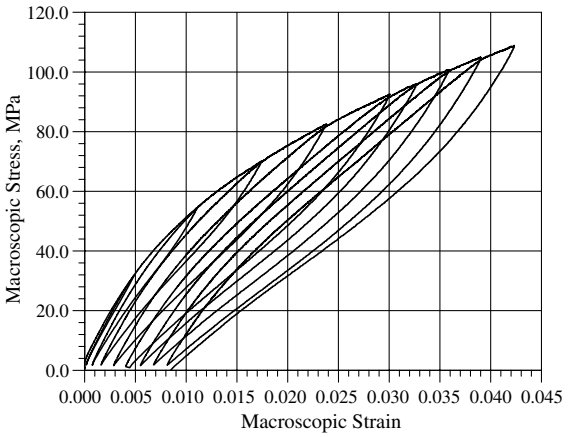

Fig. 11. Stress–strain response of small pore porous NiTi alloy tested at 60 °C.

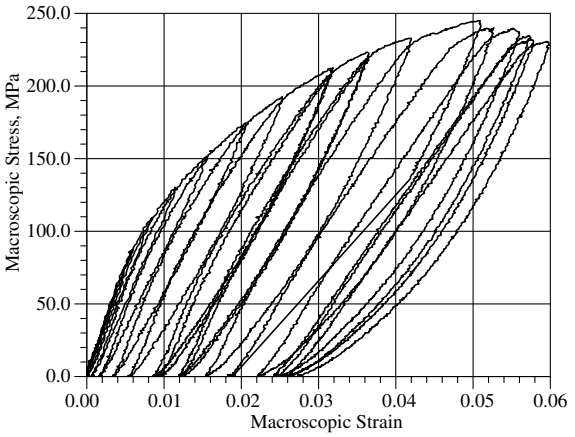

Fig. 12. Stress–strain response of large pore porous NiTi alloy tested at 60 °C.

approximate stiffness of the austenite phase in the large pore specimen is approximately 15 GPa, about twice that of the small pore austenite phase stiffness of 7 GPa. This difference in the stiffness may be partially due to incomplete diffusion of the powders in the small pore specimen and the resulting partial adherence of the powder particles. The difference in the pore volume fraction of the two types of specimens also contributes to the difference in the stiffness. Thus, while the maximum reached strain level for the two specimens is similar, the stress levels differ significantly.

When a large pore specimen is loaded to strain levels beyond 5% it starts to fail by forming microcracks, which was evident by the cracking and popping noises during loading. This failure is identified on the stress–strain curve by the decrease of the stress as the strain is increased (Fig. 12). The formation of microcracks was also confirmed after analyzing micrographs of the tested specimen after the testing, shown in Fig. 13. It can be seen that cracks form and propagate through pore walls. The residual strain after each loading/unloading step (see Fig. 14) was further analyzed. As it can be seen from Fig. 14, the residual strain follows a well-defined trend leading to saturation after the sixth loading step. Beginning with the seventh loading step, the rate of accumulation of the residual strain sharply increases. This increase can be attributed to the plastic yielding of the material

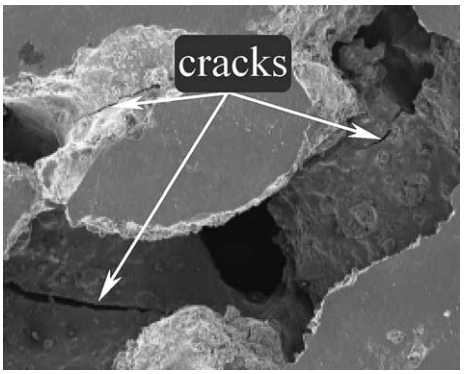

Fig. 13. Microcracking of the large pore porous NiTi SMA bar during compressive loading.

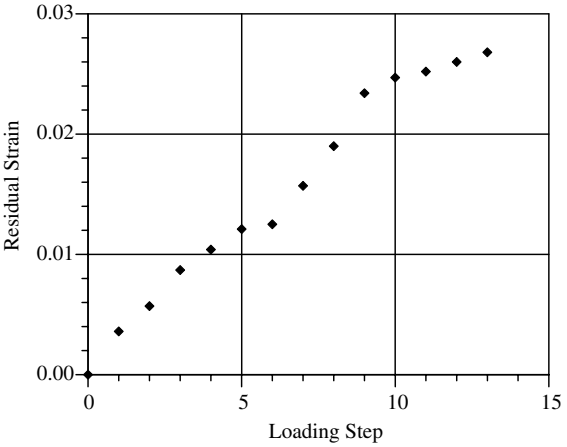

Fig. 14. Residual strain in the large pore porous NiTi SMA bar compressive loading.

in the martensitic phase without further phase transformation. This plastic yield is due to the stress concentrations at the boundaries of the pores. Thus, the combined effect of the plastic yield and the formation of microcracks is observed as formation of the second increase of the residual strain, as shown in Fig. 14.

The failure of the small pore specimens is markedly different from the one suffered by the large pore specimens. The small pore specimens failed catastrophically, forming large cracks that propagated throughout the entire specimen, causing the specimen to break into multiple fragments.

3.1. Estimation of the material properties for porous NiTi

Using the experimental data presented in Figs. 9–12 the material parameters for both types of porous NiTi alloy are estimated in this section. First, the estimation of the parameters for the small pore NiTi alloy is presented. The procedure presented here is outlined in Section I-3. Care must be exercised when taking into account the porosity. The values of the stress appearing during the estimation of the parameters in Section I-3 must be calculated for the SMA matrix. Therefore, to connect the stress in the matrix with the applied stress, the Mori–Tanaka method is used. Only one set of material parameters is obtained, since the experimental data is not sufficient to obtain complete two sets (initial and final, see Sections I-2.4 and I-3).

First the material parameters for a transformation cycle without plastic strains are estimated. To accomplish this, the residual plastic strain after each increment is subtracted from the total strain. Thus, only the elastic/phase transformation response is obtained (see Fig. 15). The material parameters are estimated for a transformation

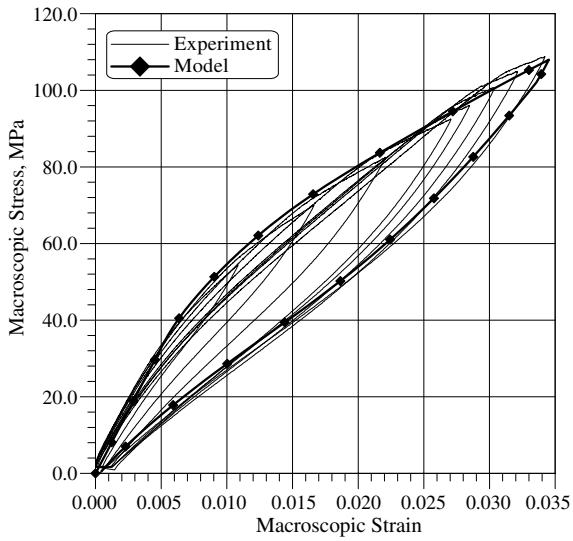

Fig. 15. Elastic/phase transformation stress–strain response of small pore porous NiTi alloy: comparison of the experimental results with the model simulations.

loop which is the envelope of the experimental results shown in Fig. 15.

To proceed with the estimation of the material properties, it is assumed that the SMA matrix is isotropic with Poisson's ratio $\nu^A = \nu^M = 0.33$. Next, the Young's elastic moduli of austenite and martensite are evaluated by solving the inverse Mori–Tanaka problem for the porous material and using the experimental data. The value of the effective Young's modulus of the porous austenite is measured using the slope at the beginning of the loading (see Fig. 15) and the corresponding value of the Young's modulus for the austenitic matrix is evaluated from the inverse Mori–Tanaka method to be $E^A = 19.7$ GPa. Similarly, the value of the effective Young's modulus of the porous martensite is obtained using the unloading slope of the last loading cycle (see Fig. 15), which results in $E^M = 19.0$ GPa. The values of the thermal expansion coefficient for martensite and austenite are taken from the work of Lagoudas and Bo (1999) and are equal to $\alpha^A = 11.0 \times 10^{-6}$ K^{-1} and $\alpha^M = 6.0 \times 10^{-6}$ K^{-1}. Similarly, the values of the specific heat constants c^A and c^M are obtained from the literature (Bo and Lagoudas, 1999). Since the loading cases considered in this work are isothermal, the last four constants will not have any effect on the numerical results, but they are still necessary for successful runs of the numerical code.

The martensitic start temperature M^{0s} is determined from the calorimetric test data, shown in Fig. 9. As explained earlier, the cooling curve in Fig. 9 shows evidence of a dual peak that is indicative of an R-phase. The second peak was used to obtain the value of the martensitic start temperatures $M^{0s} = 269.5$ K.

The experimental stress–strain curves shown in Fig. 11 differ from the stress–strain response expected for NiTi. Namely, it is expected that after initial hardening the pseudoelastic stress–strain curve reaches a plateau with subsequent hardening after the phase transformation is complete. However, the results shown in Fig. 11 reach a plateau without exhibiting the second hardening. In addition, the value of the recovered transformation strain is smaller than expected for a NiTi alloy. Therefore, these results suggest that the material does not undergo full austenite-to-martensite phase transformation. Thus, the value of the maximum transformation strain cannot be accurately obtained using the available experimental data. To overcome this difficulty a value of the maximum transformation strain $H = 3\%$ which is typical for NiTi has been used in this work. Then, it follows that the maximum value of the martensitic volume fraction ξ reached during the stress loading is approximately equal to 0.5. The value of the material parameter $\rho\Delta s_0$ is estimated to be equal to -0.03 MJ/(m^3 K) where Eq. (I-46) has been utilized by calculating the value of the stress in the matrix using the Mori–Tanaka method. The value of the material parameter Y is estimated to be equal to $Y = 1.3$ MJ/m^3.

There is no available data on the dependance of the current maximum transformation strain H^{cur} on the value of the applied stress for this alloy. Therefore, to evaluate the drag stress parameters the data for a dense NiTi alloy shown in Fig. I-6 is used with an appropriate scaling such that the maximum transformation strain for high values of stress is equal to the maximum transformation strain $H = 0.03$. The back stress parameters D_1^d, D_2^d and m_1 are evaluated by curve-fitting of the transformation stress–strain curve during forward transformation. The parameter governing the curvature of the minor transformation loops is estimated to be $\gamma = 4.0$. The comparison of the model simulations for one loop using the estimated parameters with the experimental stress–strain data is shown in Fig. 15. It can be seen that the simulation results closely match the experimental curve.

Once the parameters for a single transformation cycle are determined, the only unknowns are the parameters connected with the development of the plastic strains. To obtain the values of the parameters C_1^p and C_2^p one must have data on the evolution of plastic strain with the number of cycles. Since the loading cycles performed during the experiments are not complete, to establish the values of the parameters, a slightly different procedure than the one described in Section I-3 is used. First the model is used to establish the values of the internal parameter ζ^d at the end of each loading cycle. Next, the value of the plastic strain

at the end of each loading cycle is found from the experimental results. Thus, the relationship between the plastic strain and the accumulated detwinned martensitic volume fraction is found. Using this data and Eq. (I-51) the values of the parameters C_1^p and C_2^p are estimated. Note that the procedure presented in Section I-3 can still be utilized if complete transformation cycles were performed. The complete set of material parameters for the small pore NiTi alloy is summarized in Table 1.

The material parameters for the large pore porous NiTi alloys are estimated following the same procedure and using the data shown in Figs. 10 and 12. Only the data before the plastic yield and the formation of microcracks is used to estimate the material parameters. Some of the material parameters are identical for both the small and large pore NiTi alloys. Therefore, only the parameters which are unique for the large pore alloy are summarized in Table 2.

It is noted that the obtained material parameters for both small and large pore porous NiTi are different from the ones used earlier in Section I-2. This difference can be explained by the different processing parameters of the material. The material parameters in Section I-2 are obtained for NiTi wires, which have a substantial amount of cold work, as well as different heat treatments from the porous SMA material. In contrast, the porous SMA material has not undergone any thermomechanical treatment, such as marforming or cold work.

Table 1
Material parameters for small pore porous NiTi SMA

Physical constants	
$E^A = 19.7$ GPa	$\alpha^A = 11.0 \times 10^{-6}$ K^{-1}
$E^M = 19.0$ GPa	$\alpha^M = 6.6 \times 10^{-6}$ K^{-1}
$\rho c^A = 2.12$ MJ/(m^3 K)	$\nu = 0.33$
$\rho c^M = 2.12$ MJ/(m^3 K)	
Parameters characterizing the phase transformation	
$M^{0s} = 269.5$ K	$\rho\Delta s_0 = -0.03$ MJ/(m^3 K)
$H = 0.03$	$Y = 1.3$ MJ/m^3
$D_1^b = 7.83 \times 10^3$ MPa	$D_1^d = 2.0$ MPa
$D_2^b = -1.18 \times 10^6$ MPa	$D_2^d = -2.5$ MPa
$D_3^b = 1.01 \times 10^8$ MPa	$m_1 = 3.5$
$D_4^b = -4.19 \times 10^9$ MPa	
$D_5^b = 6.61 \times 10^{10}$ MPa	
Minor loop parameter	
$\gamma = 4.0$	
Parameters characterizing the accumulation of plastic strain	
$C_1^p = 6.0 \times 10^{-3}$	
$C_2^p = 1.66$	

Table 2
Material parameters for large pore porous NiTi SMA

Physical constants	
$E^A = 42.0$ GPa	$E^M = 32.0$ GPa
Parameters characterizing the phase transformation	
$M^{0s} = 293.0$ K	$\rho\Delta s_0 = -0.05$ MJ/(m^3 K)
$D_1^d = 12.0$ MPa	$Y = 3.0$ MJ/m^3
$D_2^d = 1.0$ MPa	
Minor loop parameter	
$\gamma = 1.0$	
Parameters characterizing the accumulation of plastic strain	
$C_1^p = 0.052$	
$C_2^p = 0.25$	

3.2. Comparison of the experimental results with model simulation

A finite element model reflecting the geometry of a typical specimen (diameter of 13 mm and length of 35 mm) is constructed. The domain is discretized using eight-node quadratic axisymmetric elements. In order to allow for both compression and combined compression–torsion loading, results of which are presented in a sequel, elements with a twist degree of freedom were used. Since the axial stress does not vary for both loading cases, only one layer of elements in the axial direction is used. The length of the elements in the axial direction is chosen to be 1.75 mm. To capture the stress variation in the radial direction, 5 elements are used. The finite element mesh and the loading history are shown in Fig. 16.

The comparison of the compressive stress–strain response for the small pore NiTi alloy simulated by the model with the experimental data is shown in Fig. 17. The material properties presented in Table 1 have been used during the numerical calculations. Overall, very good agreement between the results is obtained. Several observations are made from Fig. 17. First, the effective Young's moduli for both austenite and

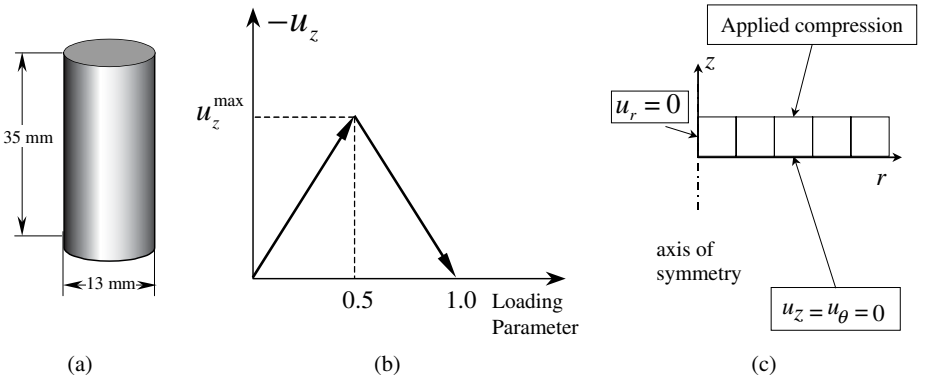

Fig. 16. Compressive loading of a porous NiTi SMA bar: (a) geometry; (b) loading history; (c) boundary conditions.

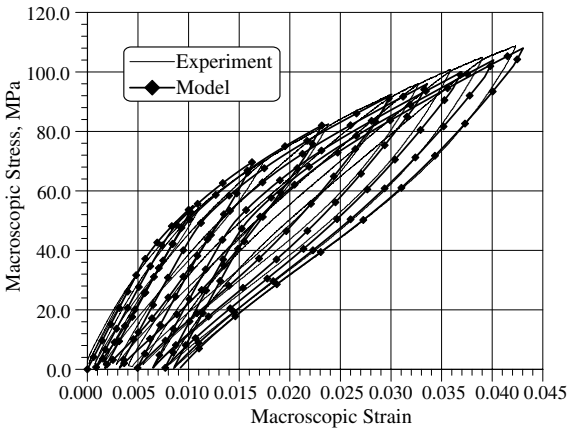

Fig. 17. Stress–strain response of a small pore porous NiTi SMA bar—comparison between the experimental results and the model simulation.

martensite are correctly reproduced by the model, since their values have been used for the model calibration. The slope of the stress–strain curve during the transformation is in good agreement with the experimental data. The behavior of the material during minor loops is also correctly reproduced.

Next, the comparison of the plastic strain predicted by the model with the plastic strain developed during the testing of the material is presented. As explained earlier, the evolution of plastic strain in the direction of the loading E^p is presented as a function of the accumulated detwinned martensitic volume fraction ζ^d. The comparison of the model simulation with the experimental data is shown in Fig. 18. It can be seen that the model simulation closely follows the experimental results.

Similar results have been calculated for the large pore porous NiTi alloy using the material parameter shown in Table 2. The comparison of the numerical results with the experimental stress–strain data is shown in Fig. 19. It can be seen that the results of the numerical simulations are in good agreement with the experimental data. The plot of the plastic strain versus the accumulated detwinned martensitic volume fraction is shown in Fig. 20.

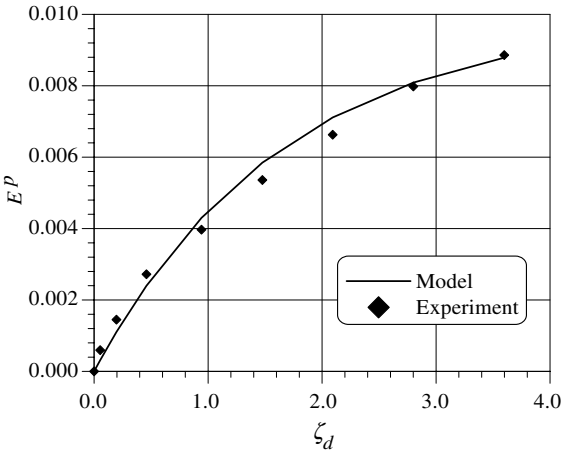

Fig. 18. Plastic strain E^p versus accumulated detwinned martensitic volume fraction ζ^d for the small pore porous NiTi.

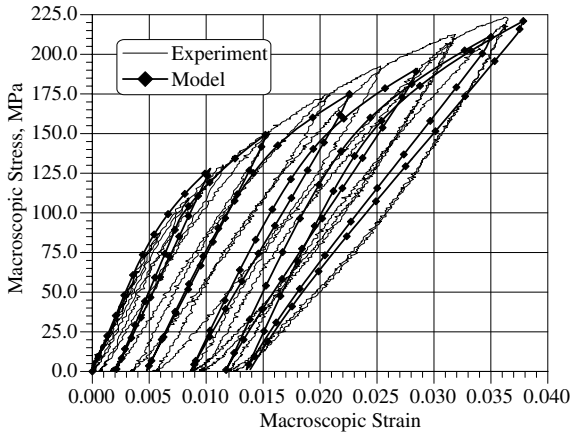

Fig. 19. Stress–strain response of a large pore porous NiTi SMA bar—comparison between the experimental results and the model simulation.

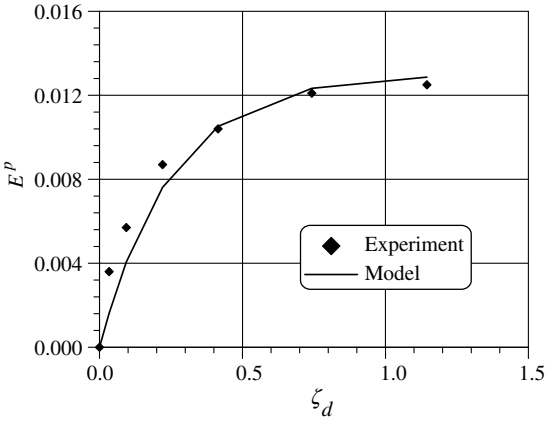

Fig. 20. Plastic strain E^{p} versus accumulated detwinned martensitic volume fraction ζ^{d} for the large pore porous NiTi.

4. Porous NiTi bars under multiaxial loading

The loading cases described above represent uniaxial loading of porous SMA bars. However, most engineering applications require the capability to handle more complex loading paths, involving multiaxial non-proportional loading. It is envisioned that the capability to model such loading cases will become increasingly important as porous SMAs are used in various new applications, such as vibration isolation of multiple degrees of freedom and biomedical applications. As an example, porous SMAs are currently considered viable material for manufacturing bone implants. Analyzing the behavior of such implants and their interaction with the living bone tissue requires capabilities to handle multiaxial loading paths. In addition, the modeling of complex loading paths will facilitate experimental work, which will provide results necessary for the calibration of the constitutive model, which is three dimensional.

To test and demonstrate the three-dimensional capabilities of the model, the response of the small pore NiTi porous SMA bar with 50% porosity, described in Section 3.1, is modeled under combined compression–torsion loading. Different loading cases were tested: compression–torsion, torsion–compression as well as simultaneous compression–torsion. The boundary conditions and the loading histories for these cases are shown in Fig. 21 while the finite element mesh is the same as shown in Fig. 16(a). The maximum value of the applied rotation (see Fig. 21) was taken to be $\theta^{\max} = 0.02$ rad ($\approx 1.15°$), which corresponds to 11.4 rad/m (1.8 full revolutions per meter) rotation, while the maximum value of the displacement in the axial direction during the second loading step was taken to be $u_z^{\max} = -0.125$ mm, corresponding to macroscopic axial compressive strain of $E_{zz} = 0.071$. Both compression and rotation boundary conditions were applied on the top surface of the specimen, while the bottom surface was held fixed in the z- and θ-directions. Traction-free boundary condition in the radial direction was applied. The numerical simulations were performed at temperature of 60 °C. The analyses were performed on a single processor DIGITAL™ Alpha 600AU workstation. Forty eight loading increments were performed to complete both loading and unloading steps and the CPU time required to perform the computations varied between 32.0 sec for the case of combined loading to 48.7 sec for the case of torsion–compression loading.

The history of the stresses and the martensitic volume fraction for the three cases are shown in Fig. 22 for an element positioned at the outer surface of the bar. It is seen that the results for the combined compression–torsion loading case resemble superposition of the results under com-

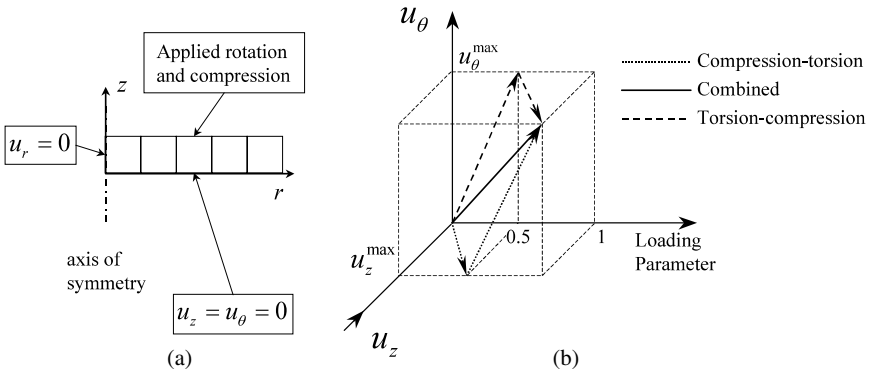

Fig. 21. Schematic of the boundary value problem (BVP) for compression–torsion multiaxial loading of a porous SMA bar: (a) boundary conditions; (b) loading histories.

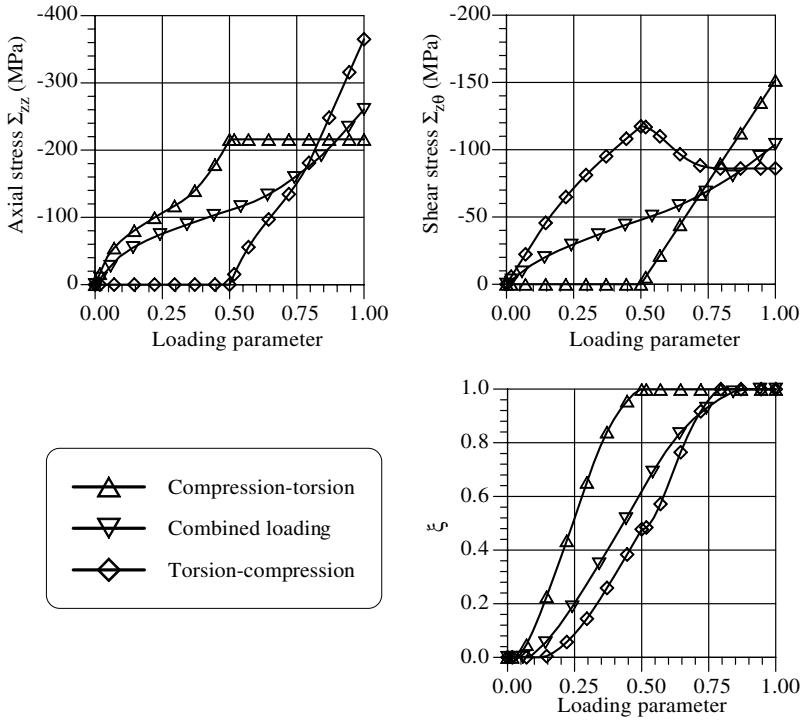

Fig. 22. History of the axial stress, shear stress and the martensitic volume fraction during multiaxial loading.

pression and torsion applied independently, while for the case of compression–torsion the material fully transforms during the compressive loading (depending on the value of the imposed axial strain) and the response under torsion is elastic. Thus only the results for the torsion–compression loading are presented in greater detail. The contour plot of the martensitic volume fraction in the SMA matrix at the end of the torsional loading (the value of loading parameter equals to 0.5) for the porous bar is shown in Fig. 23. It is observed from the figure that the contours corresponding to

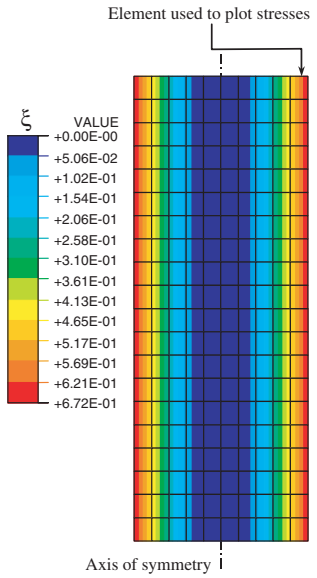

Fig. 23. Contour plot of the martensitic volume fraction in the porous NiTi SMA bar at the end of the torsional loading.

the same value of ξ are concentric circles. The maximum value of the martensitic volume fraction is $\xi = 0.67$ at the external boundary of the bar, where the shear stress is maximum, while its minimum value is $\xi = 0.0$ close to the center of the bar.

Next, the history of the stresses and the martensitic volume fraction are shown for an element positioned at the outer surface of the bar (the element is indicated in Fig. 23). For comparison purposes, the same loading case was tested on a fully dense NiTi SMA bar with the same geometry and the same material properties. The same finite element mesh of 100 quadratic axisymmetric elements as in the case of compressive loading was used. The *average* values of the axial and shear stress and the *average* value of the martensitic volume fraction versus the loading parameter for both the porous and the fully dense SMA bar are plotted on Fig. 24. It can be seen from the results that initially the porous SMA material behaves

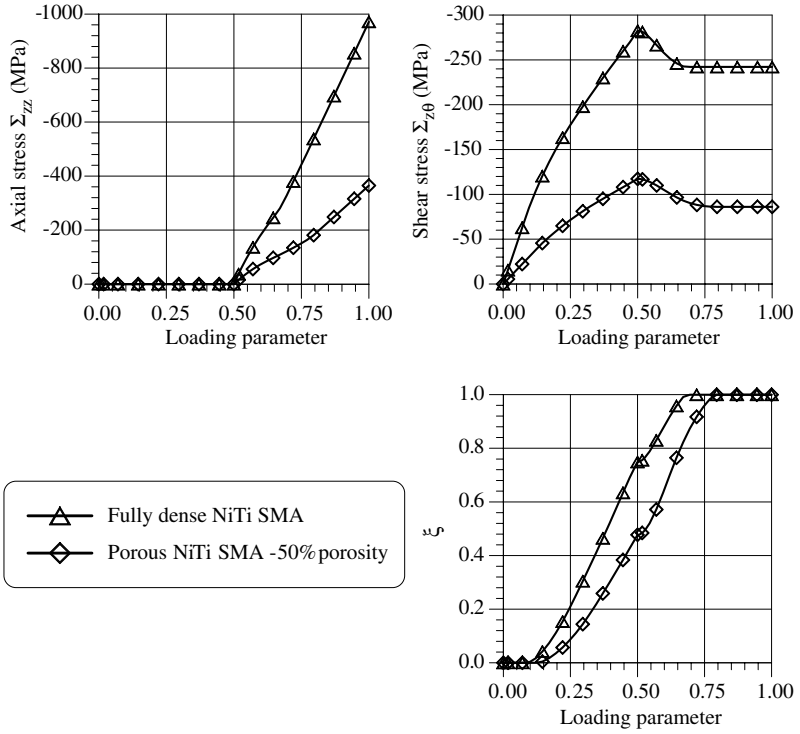

Fig. 24. History of the axial stress, shear stress and the martensitic volume fraction during torsion–compression loading.

elastically, with the onset of the phase transformation near the value for the loading parameter of about 0.15. The partial phase transformation continues to the end of the torsional loading (the value of the loading parameter is 0.5). Next, with the application of compressive loading, the phase transformation continues and it is fully completed close to the value of the loading parameter of 0.85. Due to the phase transformation during the compressive loading the shear stress $\Sigma_{z\theta}$ is partially relaxed, as indicated in Fig. 24. Upon further loading the material behaves elastically with the elastic properties of martensite. Similar trends are observed for the case of the dense SMA bar, but the stress values are much higher than the ones in the case of the porous bar.

5. Conclusions

In the current Part II of this two-part paper a micromechanical averaging model for porous SMAs, based on incremental formulation of the Mori–Tanaka method, has been presented. The micromechanical model utilizes the constitutive model for dense SMAs which has been presented in Part I of this work. Since the constitutive model for the dense SMA matrix, developed in Part I (Lagoudas and Entchev, to be published), takes into account the simultaneous evolution of transformation and plastic strains, the necessary modifications to the micromechanical model have been presented. In particular, the components of the effective inelastic strain now contain plastic strains, as shown in Section 2.3. In addition, non-linear transformation hardening, which is a result of gradual phase transformation in the SMA matrix, is also considered by the current model.

To demonstrate the three-dimensional capabilities of the model, various boundary value problems involving sequential and simultaneous compression and torsion of porous NiTi SMA bars have been analyzed. In particular, the case of sequential torsion–compression loading has been analyzed in great detail and various results have been presented.

A detailed procedure for the estimation of the material parameters for porous SMAs has been presented. The evaluation of the material parameters is given for the case of an SMA material undergoing stress-induced martensitic phase transformation. Experimental data for two different porous NiTi alloys fabricated from elemental powders have been used to estimate the material parameters. Using the estimated parameters, numerical simulations of the mechanical behavior of porous SMA bars under compression have been performed. The results of the numerical simulations have been compared with the experimental stress–strain response of the material. One drawback of using elemental powders for fabrication of porous SMAs is the lack of knowledge of material parameters for the SMA matrix. The use of prealloyed NiTi powders, which will result in better controlled material parameters, will be considered in a future work.

Acknowledgements

The help of Eric L. Vandygriff who tested the porous SMA specimens is gratefully acknowledged. The authors acknowledge the financial support of the Office of Naval Research Grant No. M00014-99-1-1069 monitored by Dr. Roshdy Barsoum and the support from the Texas Higher Education Coordinating Board TD&T Grant No. 000512-0278-1999. The authors would also like to acknowledge the Texas Institute for Intelligent Bio-Nano Materials and Structures (TiiMS) for its support. This material is based upon work supported by NASA award No. NCC-1-02038. Any opinions, findings, and conclusions or recommendations expressed in this material are those of the authors and do not necessarily reflect the views of the National Aeronautics and Space Administration.

References

Achenbach, J.D., Zhu, H., 1990. Effect of interphases on micro and macromechanical behavior of hexagonal-array fiber composites. Trans. ASME 57, 956–963.

Ayers, R.A., Simske, S.J., Bateman, T.A., Petkus, A., Sachdeva, R.L.C., Gyunter, V.E., 1999. Effects of Nitinol

implant porosity on cranial bone ingrowth and apposition after 6 weeks. J. Biomed. Mater. Res. 45 (1), 42–47.

Benveniste, Y., 1987. A new approach to the application of Mori–Tanaka's theory in composite material. Mech. Mater. 6, 147–157.

Bo, Z., Lagoudas, D.C., 1999. Thermomechanical modeling of polycrystalline SMAs under cyclic loading. Part III: Evolution of plastic strains and two-way memory effect. Int. J. Eng. Sci. 37, 1141–1173.

Bo, Z., Lagoudas, D.C., Miller, D., 1999. Material characterization of SMA actuators under nonproportional thermomechanical loading. J. Eng. Mater. Technol. 121, 75–85.

Boyd, J.G., Lagoudas, D.C., 1994. Thermomechanical response of shape memory composites. J. Intell. Mater. Syst. Struct. 5, 333–346.

Budiansky, B., 1965. On the elastic moduli of some heterogeneous materials. J. Mech. Phys. Solids 13, 223–227.

Cherkaoui, M., Sun, Q.P., Song, G.Q., 2000. Micromechanics modeling of composite with ductile matrix and shape memory alloy reinforcement. Int. J. Solids Struct. 37, 1577–1594.

Christensen, R.M., 1991. Mechanics of Composite Materials. Krieger Publishing Company, Malabar, FL.

DeGiorgi, V.G., Qidwai, M.A., 2001. Initial investigations into a polymer-porous sma composite—a computational study. In: Proceedings of ASC 16th Annual Technical Conference.

Entchev, P.B., Lagoudas, D.C., 2002. Modeling porous shape memory alloys using micromechanical averaging techniques. Mech. Mater. 34 (1), 1–24.

Gibson, L., Ashby, M., 1997. Cellular Solids. Cambridge Solid State Science Series, second ed. Cambridge University Press, Cambridge.

Green, R.J., 1972. A plasticity theory for porous solids. Int. J. Mech. Sci. 14, 215–224.

Gurson, A.L., 1977. Continuum theory of ductile rupture by void nucleation and growth. Part I: yield criteria and flow rules for porous ductile media. J. Eng. Mater. Technol. 99, 2–15.

Hershey, A.V., 1954. The elasticity of an isotropic aggregate of anisotropic cubic crystals. J. Appl. Mech. 21, 236–240.

Hill, R., 1963. Elastic properties of reinforced solids: Some theoretical principles. J. Mech. Phys. Solids 11, 357–372.

Hill, R., 1965. Continuum micromechanics of elastoplastic polycrystals. J. Mech. Phys. Solids 13, 89–101.

HKS, 1997. ABAQUS/Standard User's Manual. Hibbit, Karlsson & Sorensen, Inc., Pawtucket, RI.

Hutchinson, J.W., 1970. Elastic–plastic behaviour of polycrystalline metals and composites. Proc. Roy. Soc. Lond. A 319, 247–272.

Jeong, H.-Y., Pan, J., 1995. A macroscopic constitutive law for porous solids with pressure-sensitive matrices and its implications to plastic flow localization. Int. J. Solids Struct. 32 (24), 3669–3691.

Kröner, E., 1958. Berechnung der elastischen konstanten des vielkristalls aus den konstanten des einkristalls. Z. Phys. 151, 504–518.

Lagoudas, D.C., Bo, Z., 1999. Thermomechanical modeling of polycrystalline SMAs under cyclic loading. Part II: Material characterization and experimental results for a stable transformation cycle. Int. J. Eng. Sci. 37, 1205–1249.

Lagoudas, D.C., Bo, Z., Qidwai, M.A., 1996. A unified thermodynamic constitutive model for SMA and finite element analysis of active metal matrix composites. Mech. Compos. Mater. Struct. 3, 153–179.

Lagoudas, D.C., Boyd, J.G., Bo, Z., 1994. Micromechanics of active composites with SMA fibers. ASME J. Mater. Sci. Technol. 5, 337–347.

Lagoudas, D.C., Entchev, P.B., Qidwai, M.A., DeGiorgi, V.G., 2000. Micromechanics of porous shape memory alloys. In: Redmont, J., Main, J. (Eds.), Proceedings of 2000 ASME International Mechanical Engineering Congress and Exposition.

Lagoudas, D.C., Entchev, P.B., to be published. Modeling of transformation-induced plasticity and its effect on the behavior of porous shape memory alloys. Part I: constitutive model for fully dense SMAs. Mechanics of Materials, this issue. X-ref:10.1016/j.mechmat.2003.08.006.

Lagoudas, D.C., Gavazzi, A.C., Nigam, H., 1991. Elastoplastic behavior of metal matrix composites based on incremental plasticity and the Mori–Tanaka averaging scheme. Computat. Mech. 8, 193–203.

Lagoudas, D.C., Vandygriff, E.L., 2003. Processing and characterization of NiTi porous SMA by elevated pressure sintering. J. Intell. Mater. Syst. Struct. 13, 837–850.

Lu, Z.K., Weng, G.J., 2000. A two-level micromechanical theory for a shape-memory alloy reinforced composite. Int. J. Plasticity 16, 1289–1307.

Mori, T., Tanaka, K., 1973. Average stress in matrix and average energy of materials with misfitting inclusions. Acta Metall. 21, 571–574.

Nemat-Nasser, S., Hori, M., 1993. Micromechanics: Overall Properties of Heterogeneous Materials. North-Holland Series in Applied Mathematics and Mechanics, vol. 37. North-Holland, Amsterdam.

Qidwai, M.A., Entchev, P.B., Lagoudas, D.C., DeGiorgi, V.G., 2001. Modeling of the thermomechanical behavior of porous shape memory alloys. Int. J. Solids Struct. 38, 8653–8671.

Shabalovskaya, S.A., Itin, V.I., Gyunter, V.E., 1994. Porous Ni–Ti—a new material for implants and prostheses. In: Pelton, A.R., Hodgson, D.E., Duerig, T.W. (Eds.), Proceedings of the First International Conference on Shape Memory and Superelastic Technologies. SMST International Committee.

Simske, S.J., Ayers, R.A., Bateman, T.A., 1997. Porous materials for bone engineering. In: Liu, D.-M., Dixit, V. (Eds.), Porous Materials for Tissue Engineering. vol. 250 of Materials Science Forum. Trans Tech, Uetikon-Zurich, pp. 151–182.

Strnadel, B., Ohashi, S., Ohtsuka, H., Miyazaki, S., Ishihara, T., 1995. Effect of mechanical cycling on the pseudoelasticity characteristics of Ti–Ni and Ti–Ni–Cu alloys. Mater. Sci. Eng. A 203, 187–196.

Vandygriff, E.L., Lagoudas, D.C., Thangaraj, K., Chen, Y.-C., 2000. Porous shape memory alloys. Part I: Fabrication and characterization. In: Proceedings of ASC 15th Annual Technical Conference.

Weng, G.J., 1984. Some elastic properties of reinforced solids, with special reference to isotropic ones, containing spherical inclusions. Int. J. Eng. Sci. 22, 845–856.

Willis, J.R., 1981. Variational and related methods for the overall properties of composites. In: Yih, C.Y. (Ed.), Advances in Applied Mechanics. Academic Press, New York, pp. 1–78.

Willis, J.R., 1983. The overall elastic response of composite-materials. J. Appl. Mech. 50, 1202–1209.